Mechanistic insights into central spindle assembly mediated by the centralspindlin complex

Han Pan[a,b,1], Ruifang Guan[b,1,2], Ruixue Zhao[b,1], Guangshuo Ou[a,b,3], and Zhucheng Chen[a,b,c,3]

[a]Ministry of Education (MOE) Key Laboratory of Protein Science, Tsinghua University, Beijing 100084, People's Republic of China; [b]School of Life Science, Tsinghua University, Beijing 100084, People's Republic of China; and [c]National Institute of Biological Sciences Joint Graduate Program, Peking University, Tsinghua University, Beijing 100084, People's Republic of China

Edited by Melanie H. Cobb, University of Texas Southwestern Medical Center, Dallas, TX, and approved August 24, 2021 (received for review June 30, 2021)

The central spindle spatially and temporally regulates the formation of division plane during cytokinesis in animal cells. The heterotetrameric centralspindlin complex bundles microtubules to assemble the central spindle, the mechanism of which is poorly understood. Here, we determined the crystal structures of the molecular backbone of ZEN-4/CYK-4 centralspindlin from *Caenorhabditis elegans*, which revealed the detailed mechanism of complex formation. The molecular backbone of centralspindlin has the intrinsic propensity to undergo liquid–liquid phase separation. The condensation of centralspindlin requires two patches of basic residues at ZEN-4 and multiple acidic residues at the intrinsically disordered region of CYK-4, explaining the synergy of the two subunits for the function. These complementary charged residues were critical for the microtubule bundling activity of centralspindlin in vitro and for the assembly of the central spindle in vivo. Together, our findings provide insights into the mechanism of central spindle assembly mediated by centralspindlin through charge-driven macromolecular condensation.

centralspindlin | microtubule | cytokinesis | ZEN-4 | CYK-4

Animal cells physically separate the cellular contents at the end of cell division through cytokinesis, during which an actomyosin-based contractile ring drives ingression of the plasma membrane at the equatorial cortex (1–3). Tight spatial and temporal control of cytokinesis is essential for the proper inheritance of the genetic material into the two daughter cells. The central spindle, which forms by bundling of interpolar microtubules between the separating sister chromatids, plays an essential role in regulating when and where the cytokinesis begins (4, 5). It also gives rise to the midbody, which promotes abscission, the final phase of cytokinesis.

The formation of the central spindle depends on the centralspindlin complex in metazoans (6, 7). This complex is a constitutive heterotetramer formed by MKLP1 (ZEN-4 in *Caenorhabditis elegans*) and Cyk4 (CYK-4 in *C. elegans*) in a 2:2 manner (8). Cells lacking MKLP1 or Cyk4 cannot form the central spindle and cannot complete cytokinesis at the end, suggesting synergy between the two subunits in promoting the formation of the central spindle (9–13).

Centralspindlin contains multiple functional domains (Fig. 1*A*), playing diverse yet essential roles in cytokinesis, and it has been extensively studied in *C. elegans*. ZEN-4, a kinesin-6 family protein, includes an N-terminal motor domain, a long neck linker region, a coiled-coil (CC) dimerization domain, and a C-terminal globular domain (CTD). CYK-4 contains an N-terminal domain (NTD), a CC dimerization domain, an extended low-complex region (LCR), a membrane-binding C1 domain (14), and a RhoGAP domain. The N-terminal motor domain of ZEN-4 binds to and translocates along microtubules (15), whereas the CTD interacts with the GTPase ARF6 and the scaffold protein 14-3-3 (16–18). The LCR of CYK-4 contains multiple phosphorylation sites (19, 20), which recruit the critical guanine nucleotide exchange factor, Ect2, leading to activation of small GTPase RhoA and ultimately the formation and contraction of the actomyosin contractile ring at the cleavage furrow (21). Therefore, the multidomain centralspindlin complex bundles central spindle microtubules, regulates the signaling pathway from the central spindle to the contractile ring, and links the mitotic spindle to the plasma membrane.

ZEN-4 by itself forms a dimer, which can bind but not efficiently bundle microtubules (8). The centralspindlin complex is formed through a molecular backbone by binding the neck linker region of ZEN-4 to the NTD of CYK-4 (8, 22, 23). The neck linker is pivotal in the mechanochemical cycle of the kinesin motor by mediating the intermolecular tension between the two bound heads on the microtubule tracks (24). The neck linker of ZEN-4 has mechanistic features distinct from the canonical kinesins, in that it is unusually long (8), which is thought to reduce the intradimer head-to-head tension and stabilize the association with the microtubule tracks (25). The binding of CYK-4 to the neck linker region triggers a large-scale conformational change in the kinesin subunit, increasing the microtubule bundling activity (26).

Inside the cell, centralspindlin forms high-order clusters, which are essential for concentrating it at the central spindle and for microtubule bundling (15). Centralspindlin clustering is inhibited by the binding of 14-3-3, which is in turn antagonized by the phosphorylation of the Aurora B kinase (16, 27). In vitro, the

Significance

Centralspindlin bundles microtubules to assemble the central spindle, being essential for cytokinesis of the cell. It is a heterotetramer formed by ZEN-4 and CYK-4 in a 2:2 manner. We determined the crystal structures of centralspindlin, which revealed the detailed mechanism of complex formation. We found that centralspindlin clustered to undergo liquid–liquid phase separation (LLPS), which depended on the complementary charged residues located at ZEN-4 and CYK-4, respectively, explaining the synergy of the two subunits for the function. The LLPS of centralspindlin is critical for the microtubule bundling activity in vitro and the assembly of the central spindle in vivo. Together, our study provides angstrom-to-micron mechanistic insights into central spindle assembly mediated by the centralspindlin complex.

Author contributions: G.O. and Z.C. designed research; H.P., R.G., and R.Z. performed research; H.P., R.G., R.Z., G.O., and Z.C. analyzed data; and H.P., G.O., and Z.C. wrote the paper.

The authors declare no competing interest.

This article is a PNAS Direct Submission.

[1]H.P., R.G., and R.Z. contributed equally to this work.

[2]Present address: Laboratory of Biochemistry and Molecular Biology, National Cancer Institute, NIH, Bethesda, MD 100084.

[3]To whom correspondence may be addressed. Email: zhucheng_chen@tsinghua.edu.cn or guangshuoou@tsinghua.edu.cn.

This article contains supporting information online at https://www.pnas.org/lookup/suppl/doi:10.1073/pnas.2112039118/-/DCSupplemental.

Published September 29, 2021.

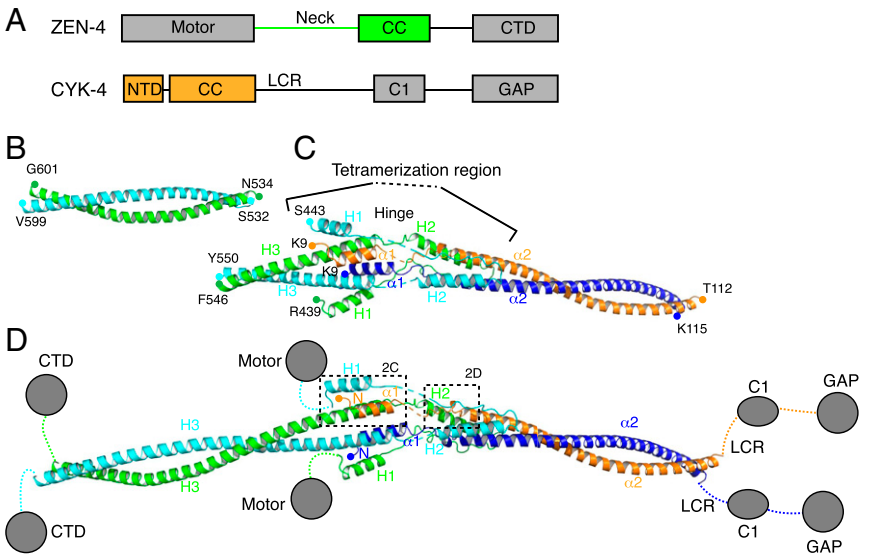

Fig. 1. Overall structure of the centralspindlin complex. (*A*) Domain architecture of ZEN-4 and CYK-4. The colored regions are used for structural determination. (*B*) Crystal structure of the CC region of ZEN-4 (residues 530 to 601). The first and last residues of the structure are labeled. (*C*) Crystal structure of the minicentralspindlin. (*D*) Composite model of the centralspindlin complex. The boxed regions are enlarged for further analysis in Fig. 2 *C* and *D*.

centralspindlin complex self-aggregates, which requires a clustering element (CE) at the end of the CC dimerization domain of ZEN-4 (15). Multimerization of centralspindlin with increased avidity is believed to promote efficient microtubule bundling and membrane binding (27).

It becomes clear that the formation of biomolecular condensates is critical in many biological systems (28). Liquid–liquid phase separation (LLPS) is known to be involved in the formation of micrometer-scale membraneless organelles. Submicron-scale condensation of macromolecules, such as centralspindlin clusters and T cell receptor clusters at the plasma membrane (29), can also generate important cellular substructures. Condensation, or phase separation, of macromolecules requires forming a network of multivalent interactions, which generally involve multiple folded domains and/or the presence of disordered regions having multiple interacting motifs (30, 31). Although it has been extensively studied, the structural basis for the centralspindlin assembly and the biophysical principles underlying centralspindlin clustering remain unclear.

Here, we determined a 2.5-Å-resolution crystal structure of a truncated form of the heterotetrameric centralspindlin complex from *C. elegans* and a 2.1-Å-resolution structure of the dimerization domain of ZEN-4 containing the CE. Together with the biochemical and genetic analyses, our findings provide insights into the assembly of the central spindle mediated by the centralspindlin complex.

Results

Overall Structure of the Centralspindlin Complex. To understand how centralspindlin assembles and clusters together, we determined the crystal structures of the dimerization domain of ZEN-4 (residues 530 to 601) and a minicentralspindlin complex formed by the neck and CC regions of ZEN-4 (residues 430 to 555) and the NTD and the CC region of CYK-4 (residues 1 to 120), Fig. 1 *B* and *C* and *SI Appendix*, Table S1. The structure of ZEN-4 (residues 530 to 601) was refined to a resolution of 2.1 Å and contains a CC dimer in an asymmetric unit (AU), Fig. 1*B*. Except for the extreme terminal ends, most of the residues were identified, including the previously identified CE (residues 586 to 601) (15), *SI Appendix*, Fig. S1*A*.

The structure of the minicomplex, which is the molecular backbone for the assembly of centralspindlin, was refined to a resolution of 2.5 Å. Two copies of the heterotetramer are in an AU (*SI Appendix*, Fig. S2*A*), which adopt similar overall conformations, particularly at the central tetramerization regions, *SI Appendix*, Fig. S2*B*. Within each of the ZEN-4 subunits, the neck linker forms two helical structures (H1 and H2) and connects to the CC dimerization domain (H3) through a flexible region, Figs. 1*C* and 2*A*. The NTD of CYK-4 forms a helix (α1) and connects to the CC dimerization domain (α2) through a loop region, Figs. 1*C* and 2*B*.

The structures of ZEN-4 (residues 530 to 601) and the minicentralspindlin share a common region (ZEN-4 residues 534 to 550). Superimposition of the common structures enabled us to build a composite model of centralspindlin, in which the CC dimerization of ZEN-4 of the minicentralspindlin extends ∼50 residues to include the known CE at the C-terminal end, Fig. 1*D*. The structure shows that the centralspindlin backbone can be delineated into two segments of helical bundles joined by a hinge region of flexible loops. One segment is the six-helix bundle formed by H1-H3-α1, which dimerizes through H3 to a total length of ∼14 nm. The neck linker region (residues 443 to 455) forms the short helix H1, suggesting that the N-terminal kinesin motor domains (residues 1 to 421) are tethered to the molecular backbone through a flexible region of ∼20 residues. The H1 helixes are located at the periphery of the six-helix bundle, which provides the structural basis for the tendency of the kinesin motor domains to be positioned on opposite sides of the molecular backbone (23). The other helical bundle is composed of H2 (ZEN-4) and α2 (CYK-4), dimerizing through α2 to a total length of ∼12 nm.

The H3 and α2 CC dimers adopt a parallel conformation and are organized into the molecular backbone in a head-to-head manner, with their N termini forming the central tetramerization region and the C termini positioned at opposite ends. These findings suggest that the multiple domains of centralspindlin are arranged along the linear molecular backbone, with the CTDs of ZEN-4 tethered at one end and the C-terminal C1 and GAP domains of CYK-4 located at the other end. The two motor domains of ZEN-4 concentrate at the central tetramerization zone, potentially cooperating in microtubule binding.

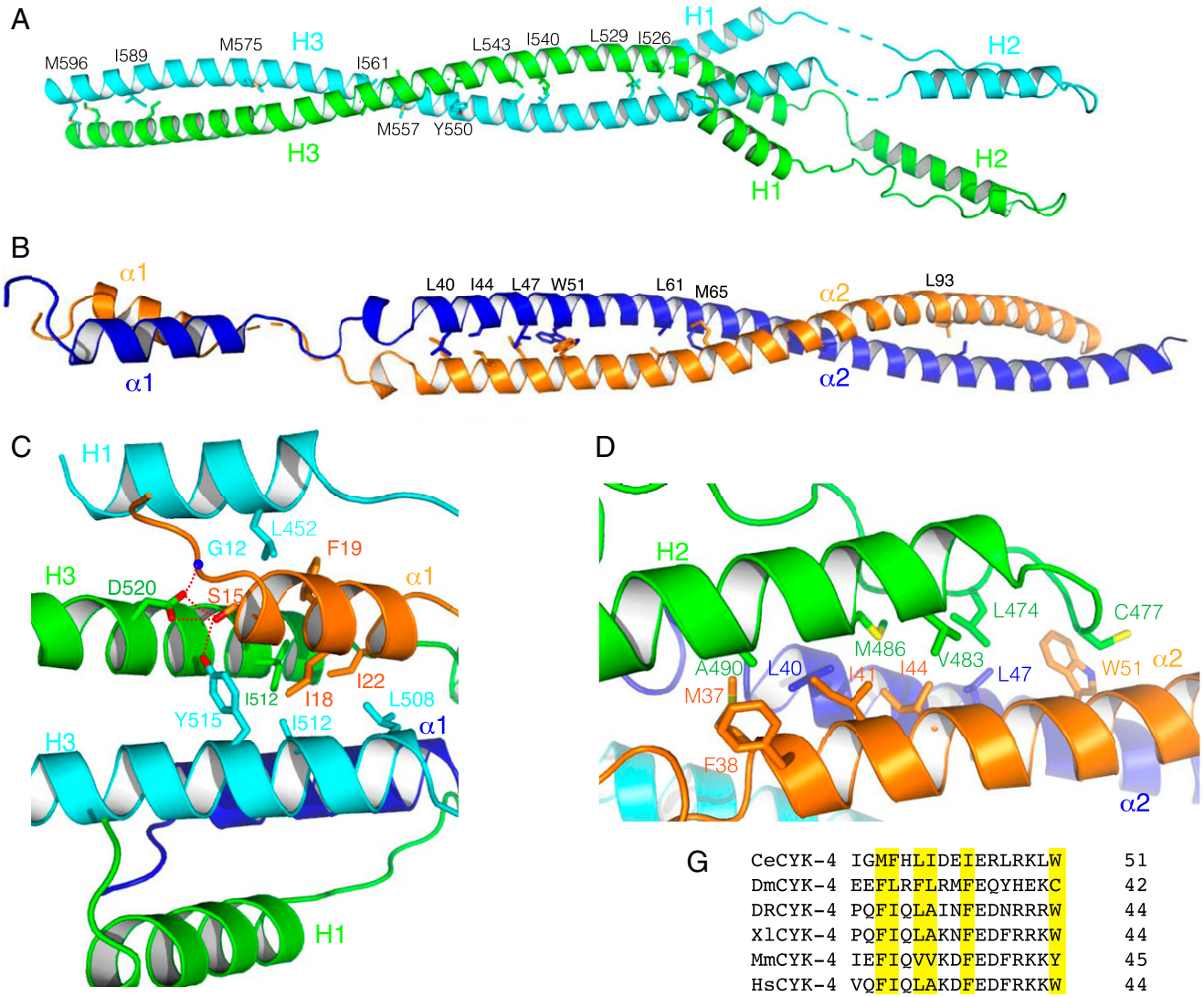

G

CeCYK-4	IGMFHLIDEIERLRKLW	51
DmCYK-4	EEFLRFLRMFEQYHEKC	42
DRCYK-4	PQFIQLAINFEDNRRRW	44
XlCYK-4	PQFIQLAKNFEDFRRKW	44
MmCYK-4	IEFIQVVKDFEDFRKKY	45
HsCYK-4	VQFIQLAKDFEDFRKKW	44

E

CeCYK-4	SRHIFNMI	22
DmCYK-4	ALASFDDL	12
DrCYK-4	LHSIFESL	15
XlCYK-4	LRNLFEQL	15
MmCYK-4	LWTLFEQL	15
HsCYK-4	VRNLFEQL	15

F

CeZEN-4	IRQYMMEADYQRV	524
DmMKLP-1	FRQMLMNLDRDNL	564
DrMKLP-1	LKSVLQEQDGNIL	548
XlMKLP-1	FRAMLQDLNGVVT	555
MmMKLP-1	FKALLKEFDNSLS	536
HsMKLP-1	FKALLQEFDNAVL	535

H

CeZEN-4	TFCLTDCNDKDTVDSMYKYA	490
DmMKLP-1	AYEMDSPEAQIKIRELMHYL	533
DrMKLP-1	PCEISGPNDDVTLPRLIEAL	517
XlMKLP-1	SCELLDANDDQSLPKLIEVL	524
MmMKLP-1	PCKLLDINDEETLPKLADTL	505
HsMKLP-1	SCEILDINDEQTLPRLIEAL	504

Fig. 2. Structural basis of ZEN-4 /CYK-4 heterotetramerization. (*A*) Structure of the ZEN-4 dimer. (*B*) Structure of the CYK-4 dimer. (*C*) Interaction between α1 of CYK-4 and ZEN-4. (*D*) Interaction between H2 of ZEN-4 and the α2 dimer of CYK-4. (*E*) Multiple sequence alignments of CYK-4 around the α1 region. Residues showing similar hydrophobic nature are highlighted in yellow and the ones conserved in magenta. (*F*) Multiple sequence alignments of ZEN-4 around the α1-binding region. Asp520 and the conserved homologs are highlighted in cyan. (*G*) Multiple sequence alignments of CYK-4 around the H2 binding region. (*H*) Multiple sequence alignments of ZEN-4 around H2.

Structural Basis of ZEN-4/CYK-4 Heterotetramerization. The primary sequences of ZEN-4 and CYK-4 homologs are not highly conserved among different species, and yet their assembly into the centralspindlin complex is well documented in metazoans (6, 7). Moreover, defects due to mutation in one subunit are suppressed by multiple substitutions in the complementary subunit, suggesting remarkable malleability of the ZEN-4/CYK-4 binding interaction (8, 22). Our structures illustrate the mechanism of centralspindlin assembly.

ZEN-4 homodimerizes mainly through hydrophobic interactions of H3, Fig. 2*A*. The residues in the dimeric interface, such as Leu529, Ile540, and Leu-543, are highly conserved, *SI Appendix*, Fig. S3. The other interfacial residues, including Ile526, Tyr550, Met557, and Ile561, are not well conserved, but the hydrophobic nature of the residues among the different homologs is evident, *SI Appendix*, Fig. S3. Likewise, the hydrophobicity of the residues in the dimeric interface of α2 is also clear in the CYK-4 homologs, Fig. 2*B* and *SI Appendix*, Fig. S4.

The H3 and α2 CC dimers are organized into the tetrameric complex through interlocking ZEN-4/CYK-4 interactions, Figs. 1*D* and 2 *C* and *D*. Two copies of α1 of the CYK-4 dimer bind to the CC region of ZEN-4 in a twofold symmetric manner, Fig. 2*C* and *SI Appendix*, Fig. S2 *C* and *D*. Reciprocally, two copies of H2 of ZEN-4 interact with the dimeric α2 of CYK-4, Fig. 2*D*.

Specifically, Ser15 of CYK-4 forms an H-bond network with Asp520 and Tyr515 of ZEN-4. Asp520 forms an additional H-bond with the main chain of Gly12 of CYK-4. Although Asp520 is mostly conserved, Ser15 of CYK-4 is unique to *C. elegans*, Fig. 2*E*, suggesting this H-bond network plays a particular role in stabilizing the binding of α1 to ZEN-4 in this model organism. In addition to the H-bond network capping the N terminus of the helix, α1 extensively interacts with ZEN-4 through multiple hydrophobic residues. Specifically, Ile18 and Ile22 pack against the side chains of Leu508, Ile512, and Tyr515 of H3. Importantly, the nonpolar nature of the interacting residues is well conserved, Fig. 2 *E* and *F*.

The structure is supported by previous biochemical and genetic observations. The S15L mutant of CYK-4 was unable to interact with ZEN-4 in vitro and led to a temperature- sensitive phenotype in *C. elegans* (8). The structure suggests that the S15L mutation disrupts the H-bond network with Asp520 and Tyr515, weakening the ZEN-4/CYK-4 interaction. Interestingly, I512F and Y515H mutations of ZEN-4 were isolated as suppressors of the S15L mutation in vivo (8). The structure suggests that the I512F and Y515H mutations probably enhanced the hydrophobic contacts to α1 of CYK-4, compensating for the loss of H-bond interactions. Likewise, the D520N mutation of ZEN-4 was defective in CYK-4 binding, but the G12D mutation of CYK-4 restored the interaction (22). These findings are consistent with the formation of an Asp520-Gly12 H-bond network between H3 and α1.

In the other half of centralspindlin, the neck linker of ZEN-4 forms the H2 helix and binds to CYK-4, with Leu474, Cys477, Val483, Met486, and Ala490 packing against the hydrophobic surface formed by α2 of CYK-4, Fig. 2*D*. This structure is consistent with the large conformational change of the neck linker of ZEN-4 upon binding to CYK-4 (26). Specifically, Leu474 of ZEN-4 is inserted into a pocket formed by Ile44, Leu47, and Trp51 of CYK-4, explaining the previous finding that the labeled L474C mutant was unable to bind CYK-4. Similar to the α1-H3 interface, the nonpolar chemical nature of the residues at the α2-H2 binding interface is largely conserved among the CYK-4 and ZEN-4 homologs, Fig. 2 *G* and *H*. Therefore, the conservation of the aliphatic nature of the homodimeric and heterotetrameric interfaces suggests that centralspindlins in other species assemble in an analogous mechanism through hydrophobic contacts although the primary sequences show variability.

The Molecular Backbone of Centralspindlin Clusters to Undergo Phase Separation. A prominent feature of centralspindlin is its low solubility in vitro, which is sensitive to the salt concentration (8). This clustering/condensation effect of centralspindlin is essential for the productive interaction with microtubules (15).

Interestingly, we found that the molecular backbone of centralspindlin (centralspindlin^{bb}) formed by ZEN-4 (430 to 601) and CYK-4 (1 to 220) clustered and underwent LLPS. In the presence of 150 mM NaCl, GFP-tagged centralspindlin^{bb} condensed into micrometer-scale droplets at a protein concentration of 2 μM, Fig. 3*A*. In line with previous studies of the endogenous complex (8), the LLPS of centralspindlin^{bb} was sensitive to the salt concentration, and no condensation was observed at 250 mM NaCl at protein concentrations up to 8 μM, suggesting charge–charge interactions play an important role in centralspindlin condensation. Droplet formation did not depend on the GFP tag, because untagged centralspindlin^{bb} also formed condensates under similar conditions, Fig. 4*A*.

The centralspindlin^{bb} droplets displayed liquid-like dynamic properties. Two droplets fused upon encounter, Fig. 3*B*, suggesting the complexes can reorganize within the droplet. Fluorescence recovery after photobleaching (FRAP) analysis showed that the complexes within the droplets underwent fluid-like exchange. The presence of the kinesin motor domain did not markedly alter the LLPS of the centralspindlin complex (Z601/C220) formed by ZEN-4 (residues 1 to 601) and CYK-4 (residues 1 to 220), with the critical concentration slightly decreasing to ∼1 μM at the physiological salt concentration, Fig. 3*D*. The Z601/C220 complex also showed dynamic behavior, Fig. 3*E*. Together, the data suggest that the molecular backbone of centralspindlin serves two purposes: it organizes the ZEN-4 and CYK-4 subunits into the heterotetrameric complex, and it drives the formation of centralspindlin condensates.

Two Patches of Positively Charged Residues of ZEN-4 Are Essential for LLPS of Centralspindlin^{bb}. To obtain mechanistic insights into the LLPS of centralspindlin^{bb}, we examined its structure in more detail. The previously identified CE (referred herein as the clustering element I, CE I), which is essential for microtubule bundling (15), was mapped to the C-terminal end of the CC of ZEN-4, Fig. 4*B*. This region is rich in positively charged residues, including Lys587, Lys594, and Arg597, which are solvent exposed, suggesting they may be involved in protein–protein interactions. To assess the importance of these residues in LLPS of centralspindlin^{bb}, we made a charge reversed mutant (Mut_I) and measured the solubility of the proteins using pelleting assays. Consistent with the phase diagram in Fig. 3*A*, wild-type (WT) centralspindlin^{bb} displayed a limited solubility in buffers containing a physiological salt concentration, with less than half of the protein remaining in the supernatant when initial samples at 10 to 16 μM were input, Fig. 4*C* and *SI Appendix*, Fig. S5*B*. In contrast, the Mut_I mutant was largely soluble, with most of the protein remaining in the supernatant even when samples at 16 μM were initially input. We confirmed the LLPS behavior of centralspindlin^{bb} using turbidity assays. Solutions of WT centralspindlin^{bb} at concentrations >2 μM became turbid, whereas solutions of the Mut_I mutant remained clear up to 16 μM, Fig. 4*D*. Furthermore, whereas the WT protein formed liquid-like droplets at a concentration of 8 μM, no droplet formed with the Mut_I mutant under the same conditions, Fig. 4*A* and *SI Appendix*, Fig. S5*A*. These findings indicate that the positively charged residues of the CE I are crucial for the LLPS of centralspindlin^{bb}.

In addition to the CE I, we found another patch of positively charged residues, including Lys542, Arg549, and Arg560, at the central region of the CC of ZEN-4, Fig. 4*B*. Similar to Mut_I, mutations of these residues (Mut_II) disrupted the LLPS of centralspindlin^{bb}, as indicated by the microscopic observations, pelleting, and turbidity assays, Fig. 4 *A*, *C*, and *D* and *SI Appendix*, Fig. S5*B*. Therefore, this positively charged region is also important for the LLPS of centralspindlin^{bb}, and we referred to it as the clustering element II (CE II).

A patch of negatively charged residues, including Glu570, Glu576, and Glu580, was located between CE I and CE II, Fig. 4*B*. Unlike CE I and CE II, mutations of these residues (3E_K) did not increase the solubility or decrease the turbidity of centralspindlin^{bb}, Fig. 4 *C* and *D* and *SI Appendix*, Fig. S5*B*, suggesting this negatively charged surface of ZEN-4 is not vital for centralspindlin^{bb} condensation. Together, the data indicate that two positively charged surfaces of the CC region of ZEN-4 play a significant role in the LLPS of centralspindlin^{bb} . Although the primary sequences of CE I and CE II are not conserved in the ZEN-4 homologs, the predicted CC regions, the human MKPL1 in particular have a net positive charge, *SI Appendix*, Fig. S3. This feature in the sequence composition suggests that the human centralspindlin complex condenses through charge–charge interactions, in line with the sensitivity of solubility to the salt concentration (15).

A Disordered Acidic Region of CYK-4 Mediates the Phase Separation of Centralspindlin. Given the salt sensitivity of the LLPS of centralspindlin^{bb}, we looked for negatively charged residues that potentially interact with the positively charged CE I and CE II. Intriguingly, CYK-4 contains a highly negatively charged region

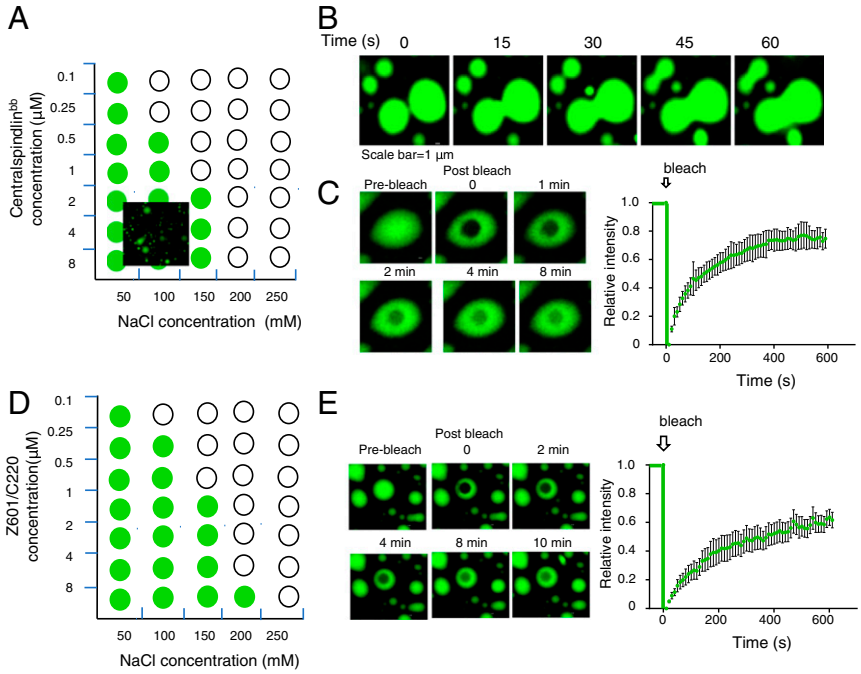

Fig. 3. LLPS of the molecular backbone of centralspindlin. (*A*) Phase diagram of the GFP-tagged centralspindlin^{bb}. Open circles, no droplet; green circles, droplets. (*Inset*) Centralspindlin^{bb} droplets. (*B*) Liquid-like fusion of the centralspindlin^{bb} droplets. (*C*) FRAP analysis of the centralspindlin^{bb} droplet. (*D*) Phase diagram of the GFP-tagged Z601/C220 centralspindlin. (*E*) FRAP analysis of the Z601/C220 centralspindlin droplet.

adjacent to the C terminus of α2, Fig. 4*E*. There are 14 acidic residues (Asp and Glu) among residues 161 to 183, a sequence that contains the known phosphorylation sites (32) and is predicted to be a disordered LCR (33). Although not as extensive as CYK-4 in *C. elegans*, the homologs in other species are also rich in acidic residues in equivalent regions, Fig. 4*F*.

To test the importance of the acidic residues, we mutated a continuous stretch of acidic residues (165 to 169) to positively charged ones (5DE). Similar to the mutations of CE I and CE II of ZEN-4, the 5DE mutation of CYK-4 noticeably increased the solubility of the complex, and the solution remained clear as shown by the microscopic observations and turbidity assays, Fig. 4 *A* and *G*, and little of the proteins were pelleted down under the conditions tested, *SI Appendix*, Fig. S5 *C* and *D*. Similar observations were made from mutations of other acidic residues distributed throughout the LCR, including E161K/D169K/D179K (EDD mutant) and D173K/D175K/E176K (DDE mutant), suggesting that multiple acidic residues of CYK-4 are involved in centralspindlin condensation. In contrast, mutations of the positively charged residues of the LCR, or mutations of the charged residues on the CC region of CYK-4, did not affect protein condensation, *SI Appendix*, Fig. S5*E*, suggesting that the distribution pattern of the charged residues is important for centralspindlin condensation. Together, these findings indicate that the negatively charged LCR of CYK-4 mediates the LLPS of centralspindlin^{bb}.

Condensation Mediated by the Molecular Backbone Is Essential for Microtubule Bundling. Having demonstrated that the positively charged CC region of ZEN-4 and the negatively charged LCR of CYK-4 mediate the LLPS of the molecular backbone of centralspindlin, we tested their impact on the microtubule bundling activity. Centralspindlin binds to microtubules mainly through the motor domains. We examined condensation of the complex with the motor domain (the Z601/C220 complex) by turbidity and microscopy assays. As expected, condensation of the Z601/C220 complex was similar to that of the molecular backbone, and the mutations that disrupted the LLPS of centralspindlin^{bb} prevented the condensation of the Z601/C220 complex, *SI Appendix*, Fig. S6 *A* and *B*. These findings suggest that the charge–charge interaction of the molecular backbone is required for the condensation of the Z601/C220 complex.

Compared with TAMRA-labeled free microtubule, the Z601/C220 complex induced formation of many bright microtubule bundles, Fig. 5*A*. In contrast, the CE I mutant (Mut_I) displayed significantly lower bundling activity, as indicated by the presence of dim unbundled microtubules. This is consistent with the previous study showing that deletion of CE I caused a defect in microtubule bundling in vitro and cytokinesis failure in vivo (15). Likewise, the CE II mutant (Mut_II) resulted in a dramatic defect in microtubule bundling. The loss of bundling activity was not due to compromised microtubule-binding affinity, because the mutant showed comparable microtubule association to that of the WT complex under the elevated salt concentration, which prevented LLPS of the complex (Fig. 3*D*) but did not affect microtubule binding, *SI Appendix*, Fig. S7*A*. Thus, as for CE I, CE II is critical for microtubule bundling of centralspindlin. In line with no disruption of the LLPS propensity, the 3E_K mutant did not perturb the microtubule bundling activity of the complex (*SI Appendix*, Fig. S6*D*).

The defect in microtubule bundling was phenocopied by the mutations of the LCR of CYK-4, Fig. 5*B*. In particular, compared with the WT complex, the 5DE mutant significantly reduced microtubule bundling, but slightly increased the microtube binding affinity (*SI Appendix*, Fig. S7*B*), probably through the removal of the acidic residues, which reduced the repulsion from the negatively charged surfaces of microtubules. Comparison with microtubules alone showed that the 5DE mutant completely abrogated the microtubule bundling activity, whereas the DDE and EDD mutants showed residual activity (*SI Appendix*, Fig. S6*C*).

To visualize the Z601/C220 complex on microtubules, we tagged ZEN-4 with a GFP fusion protein. Whereas the GFP-tagged Z601/C220 complex underwent LLPS at concentrations >1 μM as shown in Fig. 3*D*, it condensed locally along microtubule bundles at a concertation as low as 0.1 μM, which is approximately the

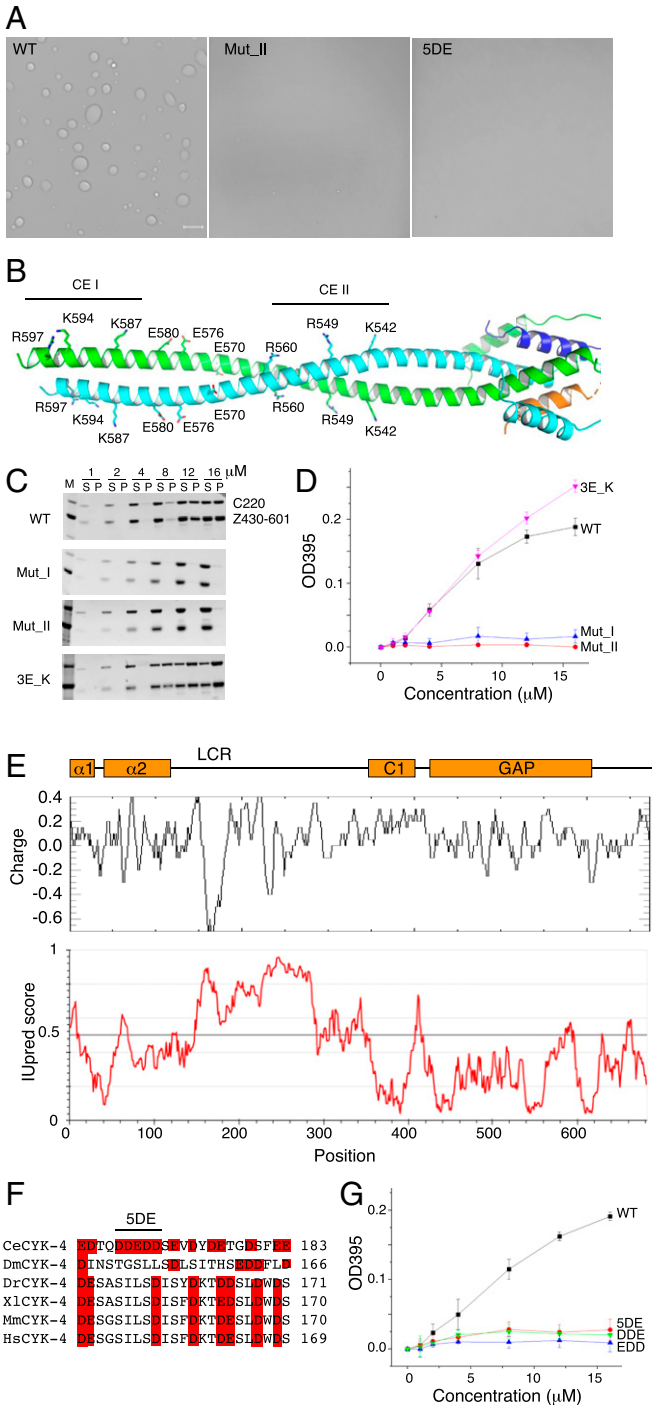

Fig. 4. Charge–charge interactions drive centralspindlin^{bb} condensation. (*A*) Droplets formed by the WT and two centralspindlin^{bb} mutants (scale bar, 10 μm). (*B*) Structure of the CC region of ZEN-4. CE I, clustering element I; CE II, clustering element II. (*C*) Pelleting assays of the WT and ZEN-4 mutant centralspindlin^{bb}. Different initial concentrations (1 to 16 μM) of centralspindlin^{bb} were used. M, molecular weight maker; S, supernatant; P, pellet. (*D*) Turbidity assays of the WT and ZEN-4 mutant centralspindlin^{bb}. Error bars indicate SD ($n = 3$). (*E*, *Top*) Schematic CYK-4 domain structure. Charge: net charge per residue with a sliding window of 10. IUpred: prediction of intrinsic disorder. (*F*) Multiple sequence alignments of CYK-4 around the acidic LCR region. Acidic residues are highlighted in red. The residues mutated in the 5DE mutant are indicated. (*G*) Turbidity assays of the WT and CYK-4 mutant centralspindlin^{bb}. Error bars indicate SD ($n = 3$).

physiological concentration inside the cell (15), Fig. 5*C*. The fluorescence intensities of the GFP-tagged Z601/C220 puncta along microtubule bundles displayed variable brightness, suggesting heterogenous amounts of the complex within the condensates. As expected, mutations of CEs prevented the formation of centralspindlin puncta on microtubules, *SI Appendix*, Fig. S6*E*. These findings suggest that centralspindlin condensation mediated by the charged residues of ZEN-4 and CYK-4 is essential for microtubule bundling.

Centralspindlin Condensation Mediated by the Molecular Backbone Is Essential for Cytokinesis. To assess the in vivo functional importance of centralspindlin condensation through the charge–charge interactions of the molecular backbone, we generated multiple independent lines of *C. elegans* that carried the knock-in Mut_II mutant of ZEN-4 (*SI Appendix*, Tables S2–S4). The heterozygotes were viable and fertile; however, the homozygous mutants displayed a partial lethal phenotype (only 3/61 of the progenies of the heterozygotes were viable). Moreover, none of the homozygous mutants produced viable offspring. Thus, the CE II element is essential for the function of centralspindlin in vivo.

We then examined the formation of the central spindle in vivo. The embryos of WT animals formed a central spindle between the separating chromatids, as indicated by the dense overlapping microtubule bundles at the midzone of the cell, which then matured into the midbody, Fig. 6*A* and Movie S1. In contrast, the homozygous Mut_II showed defective assembly of the central spindle, as indicated by the lack of overlapping microtubule bundles at the midcell, leading to cytokinesis failure and formation of multinuclear cells, Fig. 6*B*. Similarly, animals with heterozygous LCR mutations of CYK-4 (5DE) were healthy, and the homozygotes were viable but infertile, *SI Appendix*, Fig. S8 and Movie S2. Together, these findings support that centralspindlin condensation through the positively charged elements of ZEN-4 and negatively charged elements of CYK-4 is essential for cytokinesis.

Discussion

Understanding how nanoscale macromolecular machineries drive the assembly of micrometer-scale cellular structures is a key question in biology. In this study, we determined the crystal structures of the molecular backbone of the hetrotetrameric ZEN-4/CYK-4 centralspindlin complex, which provide mechanistic insights into the assembly of central spindle, Fig. 7.

The centralspindlin complex is organized by the CC regions of ZEN-4 and CYK-4, which mainly interlock through hydrophobic contacts between the NTD of CYK-4 and the neck linker region of ZEN-4. The multiple functional domains of the complex are tethered to the molecular backbone through flexible sequences. This model of the ZEN-4/CYK-4 complex, which is consistent with and integrates the findings of previous biochemical and genetic studies (8, 15, 22, 23, 26), provides a framework to understand the assembly of centralspindlin in other species.

The N-terminal kinesin motor domains are tethered to the molecular backbone through the neck linker region. The neck linker of ZEN-4, more generally in the kinesin-6 family proteins, is unusually long (~80 residues), and it interacts with CYK-4 to form centralspindlin. This interaction limits the disordered region of the neck linker to ~20 residues, constraining the distance the motor domain can reach, consistent with the previous studies (23). However, this disordered region of the neck linker is still substantially longer than the typical neck linker length of ~14 residues (24), enabling ZEN-4 to stably bind to microtubule tracks with less intermolecular tension between the two bound heads (25), in line with its primary function as a microtubule bundler.

The bundling activity of centralspindlin relies on its ability to cluster to form high-ordered oligomers (27). At the heart of the

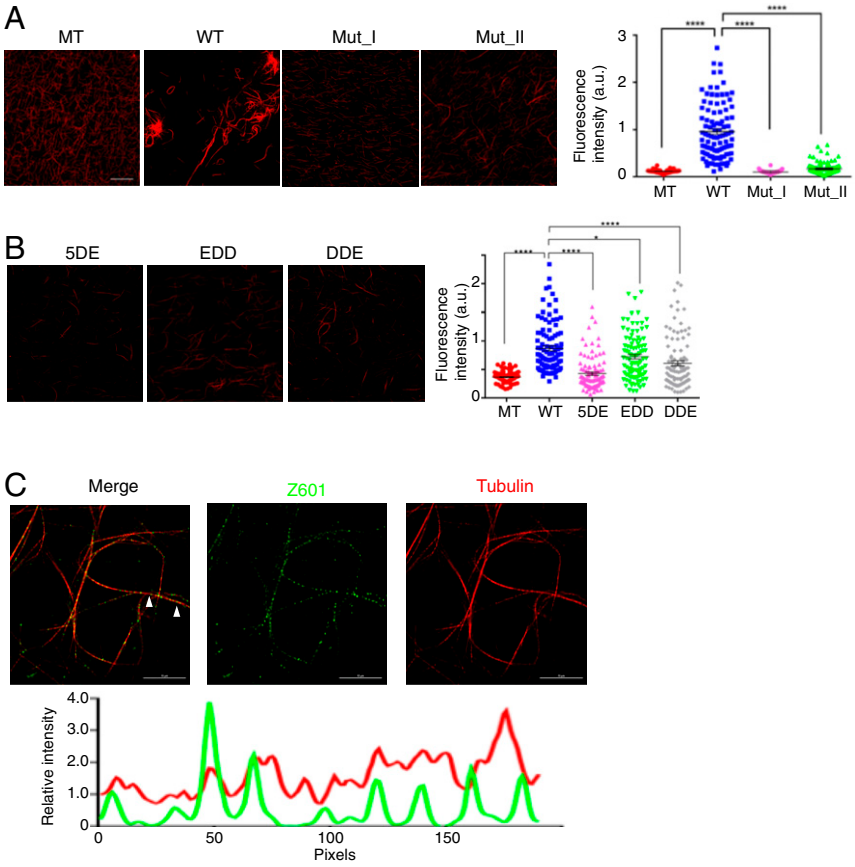

Fig. 5. Microtubule bundling mediated by centralspindlin. (*A*) Microtubule bundling mediated by the WT and ZEN-4 mutant centralspindlin (Z601/C220). Microtubules (MT) were labeled with TAMRA. Quantification of the fluorescence intensity is shown on the *Right*. Error bars indicate mean ± SEM ($n = 100$), statistical significance was determined using one-way ANOVA, ****$P < 0.0001$ (scale bar, 50 μm). (*B*) Defects in microtubule bundling of three CYK-4 mutant centralspindlin. Quantification of the fluorescence intensity was shown on the *Right*. Error bars indicate mean ± SEM ($n = 100$), statistical significance was determined using one-way ANOVA, ****$P < 0.0001$; *$P < 0.05$. (*C*) Microtubule bundling mediated by GFP-tagged centralspindlin (Z601/C220) (scale bar, 10 μm). The relative fluorescence intensity along a section of the microtubules (white arrowheads) is shown at the *Bottom*. Red, microtubule; green, GFP-tagged ZEN-4.

mechanism of centralspindlin clustering is the charge–charge interactions driven by the molecular backbone. Previous studies identified a region of ZEN-4 important for centralspindlin clustering (15). In this study, we found that it is the positively charged residues that are important for centralspindlin clustering. Moreover, we found another positively charged surface patch that is equally important for centralspindlin condensation. These basic residues are not randomly distributed along the elongated CC region of ZEN-4 but cluster at two regions, consistent with earlier studies showing that clustered charged residues promote phase separation (34). Repeated folded modular domains jointed by flexible linkers, such as SH2 and SH3 domains in Nck (35), are often found in proteins undergoing phase separation. Unlike this common theme, the rigid CC region of ZEN-4 carries the multivalent binding motifs, which may endow these kinds of macromolecule condensates with unique mechanical properties. Complementary to the positively charged ZEN-4, the LCR of CYK-4 is enriched in acidic residues and critical for centralspindlin condensation. The valency of the ZEN-4/CYK-4 interaction is increased by their homodimerization. These findings provide the physical basis for a network of charge–charge interactions required for protein condensation, which explain the salt sensitivity and the synergy of the two subunits for efficient microtubule bundling.

Our model provides a rationale for the regulation of centralspindlin condensation. The binding of the scaffold protein 14-3-3 to ZEN-4 inhibits centralspindlin condensation (16, 27). Our model suggests that 14-3-3, which is highly negatively charged (36), perturbs the charge–charge interaction between ZEN-4 and CYK-4, leading to the inhibition of complex condensation.

Centralspindlin condensates along the central spindle present favorable conditions for its functions in cells. With the molecular backbone as the core of the condensates, the increased avidity allows multiple tethering motor domains to bundle microtubules and the C1 domains to anchor the plasma membrane. Consistent with this idea, perturbation of the driving force for centralspindlin condensation was found either on the ZEN-4 or CYK-4 sides, disrupting the microtubule bundling activity in vitro and formation of the central spindle in vivo. We propose that the centralspindlin condensates facilitate efficient recruitment of the client interaction partners and cooperate with centralspindlin to bundle microtubules (37–41). The centralspindlin condensates would also generate a unique environment for downstream Ect2 signaling events. Ect2 binds to the phosphorylated LCR of CYK-4 (19, 20, 32, 42) and activates RhoA, which in turn activates nearby Ect2 molecules through a positive feedback mechanism (43–45). Ect2 contains two RhoA binding sites (43), and the multivalent interactions within the centralspindlin condensates are likely to enhance Ect2 signaling, promoting the formation of an active RhoA zone for cytokinesis. Future studies are needed to clarify the impact of centralspindlin condensates on its biological functions.

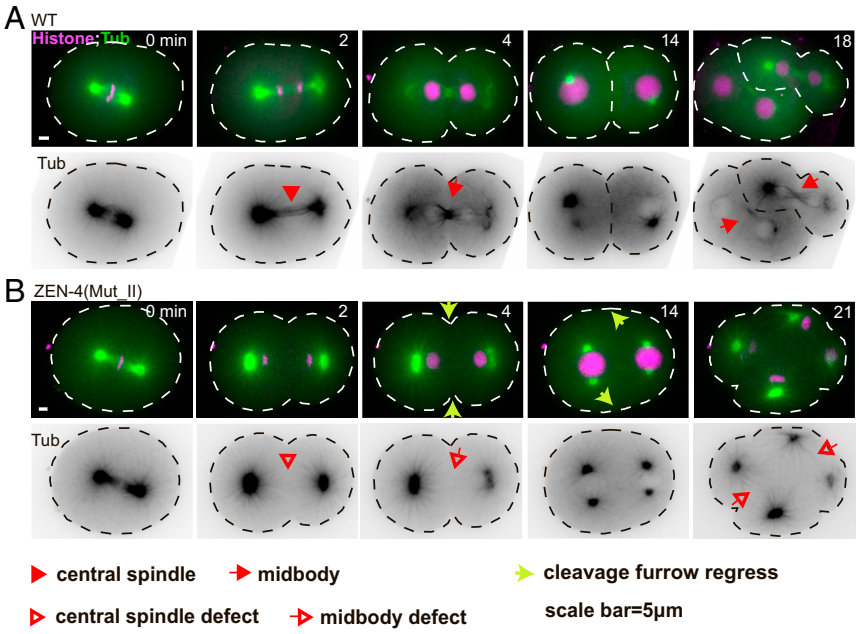

Fig. 6. The charged residues of ZEN-4 are essential for cytokinesis. (*A*) One-cell WT *C. elegans* embryos expressing mCherry::H3 and GFP::tubulin (Tub) were recorded starting at metaphase. The cell border is marked by dashed lines. (*B*) ZEN-4 Mut_II knock-in mutant showing a defect in the formation of the central spindle and failed in cytokinesis.

Experimental Procedures

Protein Expression and Purification. Genes of ZEN-4 and CYK-4 were cloned from *C. elegans* complementary DNA (cDNA). ZEN-4 was cloned into pMal-p2 vector, which had been modified with a cleavage site for TEV between the N-terminal MBP tag and the multiple cloning site (MCS), CYK-4 was cloned into pCDF-duet vector with a cleavage site for TEV between the N-terminal His tag and the MCS. Truncations of ZEN-4 and CYK-4 were generated similarly. The mutants (*SI Appendix*, Table S5) were generated by quick change PCR. GFP-tagged ZEN-4 was generated by seamless assembly cloning.

The minicentralspindlin complex (Z430-555/C120) and the dimerization domain of ZEN-4 (Z530-601) were expressed by the BL21(DE3) strain of *Escherichia coli*. Protein purification included two-step pulldown by Ni-NTA and MBP resins, after which the fusion tags were removed by TEV protease at 4 °C for about 12 h. Proteins were further purified by ion-exchange column (Source 15S, GE Healthcare) and gel-filtration chromatography (Superdex 200, GE Healthcare) and finally eluted in 200 mM NaCl, 10 mM Hepes, 5 mM DTT, pH 7.0. The purified proteins were concentrated to 15 to 20 mg/mL and stored at −80 °C.

For the molecular backbone (Z430-601/C220) and the motor-included centralspindlin complex (Z601/C220), two subunits were coexpressed in BL21(DE3) as complexes. Protein purification was similar as above, with a slight difference that proteins were finally stored in 250 mM NaCl, 10 mM Hepes, 2 mM DTT, pH 7.0 after gel-filtration purification. Various mutants and GFP-tagged complexes were expressed and purified similarly.

Crystallization and Structure Solution. Crystals of the complex Z430-555/C120 and the seleno-methionine derivative were grown at 18 °C by hanging-drop vapor diffusion methods. The crystals grew from 8 to 10% PEG3350, 100 mM NaAc 5.0, 100 mM tacsimate 5.0, 5 mM DTT. All crystals were harvested from buffer (100 mM NaCl, 12% PEG3350, 50 mM NaAc 5.0, 50 mM tacsimate 5.0). To improve the diffraction quality, the crystals were soaked in a base soak solution (100 mM NaCl, 12% PEG3350, 50 mM NaAc 5.0, 50 mM tacsimate 5.0) at 18 °C and then transferred from 0 to 24% PEG 400 in 2% increments with 10 to 15 min between each step. The soaked crystals were then flash

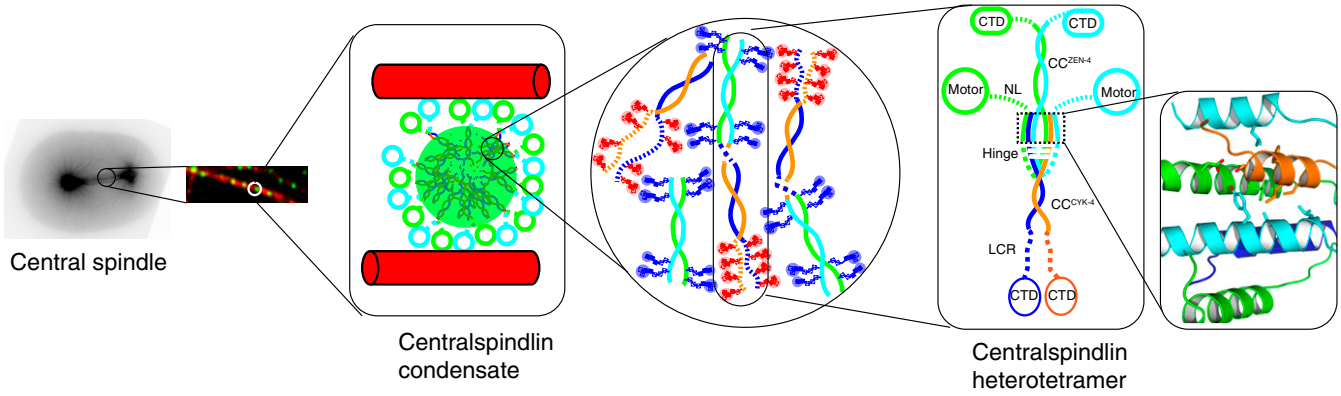

Fig. 7. Model of the formation of the central spindle mediated by centralspindlin. The centralspindlin heterotetrameric complex is assembled through the molecular backbone formed mainly via hydrophobic contacts between ZEN-4 and CYK-4. The multivalent interactions between the positively charged CC of ZEN-4 and the negatively charged LCR of CYK-4 drive the condensation of centralspindlin, which increases the avidity of the motor domains to microtubules, promoting the formation of microtubule bundles and the central spindle in cells.

frozen in liquid nitrogen for data collection. Diffraction data were collected at −170 °C at the beamline of Shanghai Synchrotron Radiation Facility (SSRF), and they were processed with the HKL2000.

Crystals of the Zen4 (530 to 601) and seleno-methionine derivative were grown at 4 °C by hanging-drop vapor diffusion methods. The crystals grew from 16% PEG2K, 200 mM $MgSO_4$, 5 mM DTT. All crystals were harvested from buffer (150 mM NaCl, 18% PEG2K, 100 mM $MgSO_4$, 20% DMSO) and flash frozen in liquid nitrogen. Diffraction data were collected at −170 °C at the beamline of SSRF, and they were processed with the HKL2000.

Initial phases were obtained by single isomorphous replacement with anomalous scattering using the program Sharp/Autosharp (46). The initial model was built with Solve/Resolve, and the rest was built manually using Coot. Model refinement was done with Phenix, with R_{work}/R_{free} = 0.2348/0.2765, Ramachandran outlier 0.13% for Z430-555/C120 and R_{work}/R_{free} = 0.2331/0.2706, Ramachandran outlier 0.0% for Z530-601.

Turbidity Assay. Turbidity assays for WT and mutant complexes (Z430-601/C220 or Z601/C220) were performed in 10 mM Hepes, 150 mM NaCl, 1mM $MgCl_2$, 1 mM DTT, 1 mM EGTA, pH 7.0, with various concentrations of ZEN-4/CYK-4 complex (0, 1, 2, 4, 8, 12, and 16 μM). Absorbance at 395 nm ($OD_{395nm,\ OD\ means\ optical\ density}$) was monitored at room temperature using a Microplate Reader (VARIOSKAN FLASH; Thermo Fisher Scientific).

Pelleting Assay and Saturation Curve. Pelleting assay was performed similarly as previously described (8). Specifically, WT and mutant (Z430-601/C220) were diluted to various concentrations (0, 1, 2, 4, 8, 12, and 16 μM) in 10 mM Hepes, 150 mM NaCl, 1 mM $MgCl_2$, 1 mM DTT, 1 mM EGTA, pH 7.0. After incubation at 20 °C for 30 min, samples were centrifuged at 17,000 *g* for 30 min at 20 °C, then the supernatant and pellet were separated for sodium dodecyl sulfate–polyacrylamide gel electrophoresis (SDS-PAGE) and Coomassie staining. Concentration of supernatant was measured by Nanodrop for each sample.

Phase Transition, Droplet Fusion, and Phase Diagram. For observation of droplet formation in vitro, samples were diluted in 10 mM Hepes, 150 mM NaCl, 1 mM $MgCl_2$, 1 mM DTT, 1 mM EGTA, pH 7.0 in the 384-well plate and were observed under Nikon A1R HD25 microscope. GFP was excited at 488 nm and detected at 500 to 550 nm.

For time-lapse microscopy of droplet fusion, samples in the 384-well plate were observed as the droplet formation assay described above, and images were acquired every 5 s for 5 min. For the phase diagram, phase transitions were observed and captured under various concentrations of protein (0.1, 0.25, 0.5, 1, 2, 4, and 8 μM) and NaCl (50, 100, 150, 200, and 250 mM).

FRAP Assay. FRAP assay was done by the Nikon A1R HD25 microscopy. Droplets of Z430-601-GFP/C220 and Z601-GFP/C220 in the 384-well plate were bleached using a laser intensity of 30% at 488 nm. Fluorescence recovery was recorded every 10 s for 10 min after bleaching. Images were acquired using NIS-Element AR software. Analyses of the fluorescence intensity of bleached regions, reference regions, and background regions were carried out by NIS-Element, and the recovery curves were drawn using Origin.

Microtubule-Bundling Assay and Quantification. Microtubule-bundling assay adopted the general method referred to in previous research with some modifications (8). For this assay, the microtubules were assembled by 5% TAMRA-labeled tubulin (TAMRA, Thermo Fisher Scientific, C1171) used in previous research (47). WT and mutant centralspindlin complexes were expressed and purified with or without GFP tags. In total, 0.1 to 0.3 μM complex was mixed with 0.1 μM TAMRA-labeled and taxol-stabilized microtubules at room temperature in Brb80 buffer (80 mM Pipes, 1 mM $MgCl_2$, 1 mM EGTA, pH 6.8) supplemented with 100 mM KCl, 50 mM NaCl, 20 μM Taxol, and 1 mM DTT and then visualized on slides with Nikon A1R HD25 microscope. GFP was excited at 488 nm and detected at 500 to 550 nm, TAMRA was excited at 561 nm and detected at 570 to 620 nm.

For quantification and statistics, the integrated intensity of TAMRA fluorescence per unit length of microtubule or microtubule bundle was measured by Image J (16, 48); 100 areas were randomly chosen from multiple micrographs to be measured and included into the GraphPad Prism statistics.

Fluorescence distribution of TAMRA-labeled microtubule bundle and GFP-tagged centralspindlin puncta were analyzed by NIS-Element and Origin.

Microtubule-Pelleting Assay. For microtubule-pelleting assay, 0.5 μM WT or mutant complex was mixed with various concentration of microtubules (0, 0.5, 1, 2, 4, 8, and 16 μM), after incubation of 20 min at room temperature, microtubules and microtubule-bound complex were spun down at 50,000 *g* for 30 min, then samples were analyzed by SDS-PAGE and Image J quantification.

Sequence Analysis for Net Charge per Residue and Low Complexity. The net charge per residue (NCPR) (https://www.bioinformatics.nl/cgi-bin/emboss/charge) and IUpred (https://iupred2a.elte.hu/) were used to analyze the charge distribution and intrinsic disorder regions of CYK-4.

The *C. elegans* Strains, Culture, and Genetics. All *C. elegans* strains were cultured at 20 °C on nematode growth medium plates seeded with the *E. coli* strain OP50 following standard protocol (49). All strains were genetically modified from WT strain Bristol N2, and *SI Appendix*, Table S3 lists strains used in this study.

Molecular Biology and Genome Editing. We performed the genome editing of *zen-4* and *cyk-4* genes in *C. elegans* following the established criteria (50, 51). The single-guide RNA (sgRNA) sequence, G(N)N19NGG (*n* = A, C, T, or G), was designed using the CRISPR design tool (https://zlab.bio/guide-design-resources). CRISPR-Cas9 targets listed in *SI Appendix*, Table S4 were inserted into the pDD162 vector (Addgene no. 47549) by linearizing pDD162 with 20 base pairs (bp) overlapped primers listed in *SI Appendix*, Table S2. For *zen-4* and *cyk-4* mutant homology recombination templates, 1.5 to 2.0 kb upstream and downstream arms were cloned into pPD95.77 plasmids with In-Fusion Advantage PCR cloning kit (Clontech, cat. no. 639621). Synonymous mutations were introduced to detect precise point mutations in the injected animals using restriction enzyme. CRISPR-Cas9 constructs and homologous recombination (HR) templates were injected into young adult worm gonad with Podr-1::dsRed and rol-6 (1006) selection markers, and marker positive F1 were screened with restriction enzyme digestion and sequencing after PCR.

Live-Cell Imaging. Live-cell imaging was performed following a previously described protocol (52). In brief, for *zen-4* mutant, we put 10 young adult worms into 2 μL M9 in a microwell dish, cut the worms with syringes to release early embryos, and mounted on 3% agarose pads. For *cyk-4* mutant, three to five young adult worms were anesthetized with 1 mg/mL levamisole and mounted on 3% agarose pads. Embryos and worms are imaged with an Axio Observer Z1 microscope (Carl Zeiss) equipped with a 100×, 1.46 numerical aperture (NA) objective lens, an electron-multiplying charge coupled device (EMCCD) camera (iXon+ DU-897D-C00-#BV-500; Andor Technology), and 488 and 568 nm lines of a Sapphire CW CDRH USB Laser System (Coherent) with a spinning disk confocal scan head (CSU-X1 Spinning Disk Unit; Yokogawa Electric Corporation). ImageJ was used to process the images.

Data Availability. Protein structure data have been deposited in the Protein Data Bank (PDB, https://www.rcsb.org/) under accession numbers 7EQB and 7EQC. All other data are available from the corresponding author upon reasonable request.

ACKNOWLEDGMENTS. We are also thankful to Michael Glotzer for discussing the literature related to the centralspindlin crystal structure. We thank the staff at the Center of Structure Biology (Tsinghua University) and beamline BL17U of SSRF for help with diffraction data collection, and Xin Liang for providing TAMRA-labeled tubulin. This work was supported by the National Key Research and Development Program (2019YFA0508902 and 2017YFA0102900 to Z.C.), the National Natural Science Foundation of China (31825016 and 31630046 to Z.C.), the National Key R&D Programof China (2019YFA0508401 to G.O.), and Advanced Innovation Center for Structural Biology, Tsinghua-Peking Joint Center for Life Sciences.

1. T. D. Pollard, B. O'Shaughnessy, Molecular mechanism of cytokinesis. *Annu. Rev. Biochem.* **88**, 661–689 (2019).
2. U. S. Eggert, T. J. Mitchison, C. M. Field, Animal cytokinesis: From parts list to mechanisms. *Annu. Rev. Biochem.* **75**, 543–566 (2006).
3. F. A. Barr, U. Gruneberg, Cytokinesis: Placing and making the final cut. *Cell* **131**, 847–860 (2007).
4. M. E. Douglas, M. Mishima, Still entangled: Assembly of the central spindle by multiple microtubule modulators. *Semin. Cell Dev. Biol.* **21**, 899–908 (2010).
5. M. Glotzer, The 3Ms of central spindle assembly: Microtubules, motors and MAPs. *Nat. Rev. Mol. Cell Biol.* **10**, 9–20 (2009).
6. M. Mishima, Centralspindlin in Rappaport's cleavage signaling. *Semin. Cell Dev. Biol.* **53**, 45–56 (2016).
7. E. A. White, M. Glotzer, Centralspindlin: At the heart of cytokinesis. *Cytoskeleton (Hoboken)* **69**, 882–892 (2012).
8. M. Mishima, S. Kaitna, M. Glotzer, Central spindle assembly and cytokinesis require a kinesin-like protein/RhoGAP complex with microtubule bundling activity. *Dev. Cell* **2**, 41–54 (2002).

9. J. Powers, O. Bossinger, D. Rose, S. Strome, W. Saxton, A nematode kinesin required for cleavage furrow advancement. *Curr. Biol.* **8**, 1133–1136 (1998).
10. W. B. Raich, A. N. Moran, J. H. Rothman, J. Hardin, Cytokinesis and midzone microtubule organization in *Caenorhabditis elegans* require the kinesin-like protein ZEN-4. *Mol. Biol. Cell* **9**, 2037–2049 (1998).
11. R. R. Adams, A. A. Tavares, A. Salzberg, H. J. Bellen, D. M. Glover, Pavarotti encodes a kinesin-like protein required to organize the central spindle and contractile ring for cytokinesis. *Genes Dev.* **12**, 1483–1494 (1998).
12. V. Jantsch-Plunger *et al*., CYK-4: A Rho family gtpase activating protein (GAP) required for central spindle formation and cytokinesis. *J. Cell Biol.* **149**, 1391–1404 (2000).
13. P. Gönczy *et al*., Dissection of cell division processes in the one cell stage Caenorhabditis elegans embryo by mutational analysis. *J. Cell Biol.* **144**, 927–946 (1999).
14. S. Lekomtsev *et al*., Centralspindlin links the mitotic spindle to the plasma membrane during cytokinesis. *Nature* **492**, 276–279 (2012).
15. A. Hutterer, M. Glotzer, M. Mishima, Clustering of centralspindlin is essential for its accumulation to the central spindle and the midbody. *Curr. Biol.* **19**, 2043–2049 (2009).
16. M. E. Douglas, T. Davies, N. Joseph, M. Mishima, Aurora B and 14-3-3 coordinately regulate clustering of centralspindlin during cytokinesis. *Curr. Biol.* **20**, 927–933 (2010).
17. H. Makyio *et al*., Structural basis for Arf6-MKLP1 complex formation on the Flemming body responsible for cytokinesis. *EMBO J.* **31**, 2590–2603 (2012).
18. N. Joseph, A. Hutterer, I. Poser, M. Mishima, ARF6 GTPase protects the post-mitotic midbody from 14-3-3-mediated disintegration. *EMBO J.* **31**, 2604–2614 (2012).
19. B. A. Wolfe, T. Takaki, M. Petronczki, M. Glotzer, Polo-like kinase 1 directs assembly of the HsCyk-4 RhoGAP/Ect2 RhoGEF complex to initiate cleavage furrow formation. *PLoS Biol.* **7**, e1000110 (2009).
20. M. E. Burkard *et al*., Plk1 self-organization and priming phosphorylation of HsCYK-4 at the spindle midzone regulate the onset of division in human cells. *PLoS Biol.* **7**, e1000111 (2009).
21. A. Basant, M. Glotzer, Spatiotemporal regulation of RhoA during cytokinesis. *Curr. Biol.* **28**, R570–R580 (2018).
22. V. Pavicic-Kaltenbrunner, M. Mishima, M. Glotzer, Cooperative assembly of CYK-4/MgcRacGAP and ZEN-4/MKLP1 to form the centralspindlin complex. *Mol. Biol. Cell* **18**, 4992–5003 (2007).
23. T. Davies *et al*., CYK4 promotes antiparallel microtubule bundling by optimizing MKLP1 neck conformation. *PLoS Biol.* **13**, e1002121 (2015).
24. S. Shastry, W. O. Hancock, Interhead tension determines processivity across diverse N-terminal kinesins. *Proc. Natl. Acad. Sci. U.S.A.* **108**, 16253–16258 (2011).
25. R. Guan *et al*., Crystal structure of Zen4 in the apo state reveals a missing conformation of kinesin. *Nat. Commun.* **8**, 14951 (2017).
26. E. A. White, H. Raghuraman, E. Perozo, M. Glotzer, Binding of the CYK-4 subunit of the centralspindlin complex induces a large scale conformational change in the kinesin subunit. *J. Biol. Chem.* **288**, 19785–19795 (2013).
27. A. Basant *et al*., Aurora B kinase promotes cytokinesis by inducing centralspindlin oligomers that associate with the plasma membrane. *Dev. Cell* **33**, 204–215 (2015).
28. S. F. Banani, H. O. Lee, A. A. Hyman, M. K. Rosen, Biomolecular condensates: Organizers of cellular biochemistry. *Nat. Rev. Mol. Cell Biol.* **18**, 285–298 (2017).
29. X. Su *et al*., Phase separation of signaling molecules promotes T cell receptor signal transduction. *Science* **352**, 595–599 (2016).
30. S. Boeynaems *et al*., Protein phase separation: A new phase in cell biology. *Trends Cell Biol.* **28**, 420–435 (2018).
31. H. Zhang *et al*., Liquid-liquid phase separation in biology: Mechanisms, physiological functions and human diseases. *Sci. China Life Sci.* **63**, 953–985 (2020).
32. J. S. Gómez-Cavazos *et al*., A non-canonical BRCT-phosphopeptide recognition mechanism underlies RhoA activation in cytokinesis. *Curr. Biol.* **30**, 3101–3115.e11 (2020).
33. B. Mészáros, G. Erdos, Z. Dosztányi, IUPred2A: Context-dependent prediction of protein disorder as a function of redox state and protein binding. *Nucleic Acids Res.* **46**, W329–W337 (2018).
34. T. J. Nott *et al*., Phase transition of a disordered nuage protein generates environmentally responsive membraneless organelles. *Mol. Cell* **57**, 936–947 (2015).
35. P. Li *et al*., Phase transitions in the assembly of multivalent signalling proteins. *Nature* **483**, 336–340 (2012).
36. D. K. Morrison, The 14-3-3 proteins: Integrators of diverse signaling cues that impact cell fate and cancer development. *Trends Cell Biol.* **19**, 16–23 (2009).
37. R. Ban, Y. Irino, K. Fukami, H. Tanaka, Human mitotic spindle-associated protein PRC1 inhibits MgcRacGAP activity toward Cdc42 during the metaphase. *J. Biol. Chem.* **279**, 16394–16402 (2004).
38. K. Y. Lee, B. Esmaeili, B. Zealley, M. Mishima, Direct interaction between centralspindlin and PRC1 reinforces mechanical resilience of the central spindle. *Nat. Commun.* **6**, 7290 (2015).
39. R. Subramanian *et al*., Insights into antiparallel microtubule crosslinking by PRC1, a conserved nonmotor microtubule binding protein. *Cell* **142**, 433–443 (2010).
40. M. Mishima, K. Y. Lee, Central spindle robustness by PRC1-centralspindlin interaction. *Cell Cycle* **14**, 3515–3516 (2015).
41. K. J. Verbrugghe, J. G. White, SPD-1 is required for the formation of the spindle midzone but is not essential for the completion of cytokinesis in *C. elegans* embryos. *Curr. Biol.* **14**, 1755–1760 (2004).
42. Y. Zou *et al*., Crystal structure of triple-BRCT-domain of ECT2 and insights into the binding characteristics to CYK-4. *FEBS Lett.* **588**, 2911–2920 (2014).
43. M. Chen *et al*., Structure and regulation of human epithelial cell transforming 2 protein. *Proc. Natl. Acad. Sci. U.S.A.* **117**, 1027–1035 (2020).
44. D. Zhang, M. Glotzer, The RhoGAP activity of CYK-4/MgcRacGAP functions noncanonically by promoting RhoA activation during cytokinesis. *eLife* **4**, e08898 (2015).
45. W. M. Bement *et al*., Activator-inhibitor coupling between Rho signalling and actin assembly makes the cell cortex an excitable medium. *Nat. Cell Biol.* **17**, 1471–1483 (2015).
46. C. Vonrhein, E. Blanc, P. Roversi, G. Bricogne, Automated structure solution with autoSHARP. *Methods Mol. Biol.* **364**, 215–230 (2007).
47. Y. Song *et al*., The microtubule end-binding affinity of EB1 is enhanced by a dimeric organization that is susceptible to phosphorylation. *J. Cell Sci.* **133**, jcs241216 (2020).
48. Y. Zhu, W. Tan, W. L. Lee, An *in vitro* microscopy-based assay for microtubule-binding and microtubule-crosslinking by budding yeast microtubule-associated protein. *Bio Protoc.* **8**, e3110 (2018).
49. S. Brenner, The genetics of *Caenorhabditis elegans*. *Genetics* **77**, 71–94 (1974).
50. D. J. Dickinson, J. D. Ward, D. J. Reiner, B. Goldstein, Engineering the *Caenorhabditis elegans* genome using Cas9-triggered homologous recombination. *Nat. Methods* **10**, 1028–1034 (2013).
51. A. E. Friedland *et al*., Heritable genome editing in *C. elegans* via a CRISPR-Cas9 system. *Nat. Methods* **10**, 741–743 (2013).
52. Y. Chai *et al*., Live imaging of cellular dynamics during *Caenorhabditis elegans* postembryonic development. *Nat. Protoc.* **7**, 2090–2102 (2012).